CrystEngComm

PAPER

View Article Online
View Journal | View Issue

Cite this: *CrystEngComm*, 2016, **18**, 1000

Hollow nanocrystals of silicoaluminophosphate molecular sieves synthesized by an aminothermal co-templating strategy†

Dehua Wang,[ab] Miao Yang,[a] Wenna Zhang,[ab] Dong Fan,[ab] Peng Tian*[a] and Zhongmin Liu*[a]

Received 9th September 2015,
Accepted 4th January 2016

DOI: 10.1039/c5ce01798j

www.rsc.org/crystengcomm

An aminothermal co-templating strategy has been developed to explore the synthesis of SAPO molecular sieves. Nanosized SAPO-56 (AFX) with a hollow morphology is, for the first time, obtained by utilizing triethylamine (TEA) and trimethylamine (TMA) as both the solvent and the template in the presence of HF. The prepared material is well characterized, and the coexistence of TEA and TMA in the crystals is proved by ^{13}C NMR. Molecular modelling indicates that the most stable status for the as-made SAPO-56 is 2TEA per *aft* cage and 1TMA per *gme* cage in the AFX structure, which is consistent with the TG results and verifies the co-templating behaviour of the two amines. In addition, the aminothermal crystallization process of SAPO-56 is examined, revealing an interesting *in situ* phase transformation from SAPO-34 (only containing TEA) to nano SAPO-56 followed by a further *in situ* post-synthetic leaching to achieve the hollow structure. Both F^- anions and organic amines are proposed to be responsible for the dissolution of SAPO-34 and the etching of SAPO-56 nanocrystals. The Si-rich outer layer with abundant Si coordination environments (more Si–O–Al bonds and less Al–O–P bonds) helps the shell of SAPO-56 survive the leaching. This work offers an effective way to prepare SAPO-56 nanocrystals and demonstrates the huge potential of the aminothermal co-templating route for new material synthesis.

1 Introduction

Molecular sieves are microporous crystalline materials with large surface area, good thermal/hydrothermal stability and tunable acidity, which have found widespread applications in the chemical industry as catalysts, adsorbents, and ion exchangers.[1,2] Their excellent properties are highly dependent on their unique framework topologies, composition and morphology. The growing environmental and technological needs for molecular sieves in applications inspire researchers to explore new synthetic methodologies and materials with desired structures and physicochemical properties.

It has been recognized that an organic structure-directing agent (SDA) is of vital importance to control the structure and properties of the final product.[3] Although precise prediction of a template for a desired structure still remains a challenge, the use of novel amines as a SDA has been proven to be an effective way to create new molecular sieves. The most famous examples are the successful syntheses of serial SSZ and ITQ zeolites with designed SDAs reported by Zones *et al.* and Corma *et al.*, respectively.[4–6] Moreover, even with common amines, the innovation of new synthetic methods, such as solvothermal and ionothermal syntheses, also bring opportunities to achieve materials with novel structures and special properties.[7,8] The solvothermal or ionothermal environment different from the hydrothermal one is believed to exert an influence on the synthesis and contribute to the formation of novel materials.

The co-templating strategy, in which two or more amines are employed, is an interesting route to synthesize molecular sieves. It can be used to tune the morphology and microstructure of molecular sieves. Many cases may be found in the synthesis of SAPO-34 by mixed SDAs,[9,10] which is currently the most excellent catalyst for the methanol-to-olefins reaction.[11] More importantly, the co-templating method shows promising ability to synthesize new aluminosilicate zeolites[5,12] and their aluminophosphate[13,14] and silicoaluminophosphate (SAPO)[15] analogues. For example, an aluminophosphate $AlPO_4$-CLO (named as DNL-1) with a 20-ring extra-large pore structure and good thermal stability was synthesized by introducing tetramethylammonium (TMA^+) into the ionothermal system of $AlPO_4$ synthesis.[8] The different sized *lta* cage and *sod* cage belonging to the –CLO structure are

[a] *National Engineering Laboratory for Methanol to Olefins, Dalian National Laboratory for Clean Energy, Dalian Institute of Chemical Physics, Chinese Academy of Sciences, Zhongshan Road No. 457, Dalian 116023, PR China. E-mail: tianpeng@dicp.ac.cn, liuzm@dicp.ac.cn*

[b] *Graduate University of Chinese Academy of Sciences, Beijing 100049, PR China*

† Electronic supplementary information (ESI) available. See DOI: 10.1039/c5ce01798j

found to be filled with 1-benzyl-3-methylimidazolium cations ($BenzMIM^+$) and TMA^+, respectively, which illustrates the powerful effect of the cooperation between amines. In addition, SAPO molecular sieves with SAV, KFI and FAU topologies are also hydrothermally synthesized by using a co-templating route.[15,16] Given that most of the structures only achieved by co-amines contain two types of cages, it is reasonable to conclude that the co-templating approach has a unique advantage for directing a structure having more than one cage type, where different cage structures are stabilized by different amines with certain size and charge density.[12,16,17]

One possible problem with the co-templating strategy is the phase separation in the synthetic system, that is, no co-operation between SDAs is achieved. Therefore, synthetic conditions and the combination of amines should be carefully controlled to reach a desired aim. Researchers at UOP once proposed a charge density mismatch (CDM) approach to avoid this problem,[18,19] which was initially developed as a cheaper alternative to the expensive and complicated SDAs. The method involves the first preparation of a solution having a relatively low Si/Al ratio by using large quaternary ammonium (low charge density). Because the large SDA cannot efficiently balance the highly negative aluminosilicate species, crystallization in the solution is difficult to occur. A small amount of high charge density SDAs (small size) is then introduced to the solution to initiate the crystallization. The complementary advantages of these SDAs in the dosage and directing ability prompt them to cooperate with each other to complete the crystallization.

In our previous work, a novel aminothermal process, using organic amine as both the solvent and the template, has been developed to synthesize SAPO molecular sieves.[20,21] It is found that amines in the aminothermal environment may show different directing behaviors from the cases under hydrothermal conditions.[22,23] In addition, aminothermally synthesized SAPO-34 with high Si content exhibits excellent CO_2 adsorption capacity and high CO_2/N_2 selectivity.[22] Inspired by these experimental results together with the above-mentioned co-template research, we therefore concentrate our efforts to investigate the co-templating synthesis of SAPO molecular sieves in the aminothermal environment. Herein, as a preliminary trial, triethylamine (TEA) and small molecule trimethylamine (TMA), the two most common organic amines, are employed as the solvent/template and co-template, respectively. Fortunately, interesting results have been achieved.

2 Experimental

2.1 Synthesis

Organic amines used in the synthesis were TEA (99.5 wt%) and TMA aqueous solution (33 wt%). Silica sol (31 wt%), pseudoboehmite (72.5 wt%), phosphoric acid (85 wt%), and HF aqueous solution (40 wt%) were used as inorganic reactants.

A typical synthesis procedure was as follows: triethylamine, pseudoboehmite and silica sol were added in sequence into a glass beaker. After stirring for 10 min, phosphoric acid and trimethylamine were subsequently added dropwise into the mixture with stirring. A homogeneous and viscous mixture was obtained and transferred to an autoclave. Then HF solution was added into the above obtained solution with strong agitation to obtain the final gel, following which the mixture was sealed quickly and placed in an oven. After the autoclave was rotated at 50 rpm for 30 min to obtain a more homogeneous mixture, it was heated at 200 °C under rotation and kept for a certain time. At the end of the crystallization, the products were recovered by filtration with distilled water and dried at 100 °C in air. The as-synthesized materials were calcined in air at 550 °C for 4 h to obtain the template-free samples.

2.2 Characterization

The powder XRD patterns were recorded on a PANalytical X'Pert PRO X-ray diffractometer with Cu-Kα radiation (λ = 1.54059 Å), operating at 40 kV and 40 mA. The chemical composition of the samples was determined using a Philips Magix-601 X-ray fluorescence (XRF) spectrometer. The crystal morphology was observed by using field emission scanning electron microscopy (SU8020). Transmission electron microscopy (TEM) images were obtained using a JEM-2100 electron microscope. All the solid state NMR experiments were performed using a Bruker Avance III 600 spectrometer equipped with a 14.1 T wide-bore magnet. The resonance frequencies were 150.9, 156.4, 242.9 and 119.2 MHz for ^{13}C, ^{27}Al, ^{31}P and ^{29}Si, respectively. ^{13}C, ^{27}Al and ^{31}P MAS NMR experiments were performed using a 4 mm MAS probe with a spinning rate of 12 kHz. ^{13}C MAS NMR spectra were recorded with a contact time of 3 ms and a recycle delay of 4 s. ^{27}Al MAS NMR spectrum was recorded using a one pulse sequence. 200 scans were accumulated with a $\pi/8$ pulse width of 0.75 μs and a 2 s recycle delay. Chemical shifts were referenced to $(NH_4)Al(SO_4)_2{\cdot}2H_2O$ at −0.4 ppm. ^{31}P MAS NMR spectrum was recorded using high-power proton decoupling. 32 scans were accumulated with a $\pi/4$ pulse width of 2.25 μs and a 10 s recycle delay. Chemical shifts were referenced to 85% H_3PO_4 at 0 ppm. ^{29}Si MAS NMR spectrum was recorded using a 7 mm MAS probe with a spinning rate of 6 kHz using high-power proton decoupling. 5000–6000 scans were accumulated with a $\pi/4$ pulse width of 2.5 μs and a 10 s recycle delay. Chemical shifts were referenced to 4,4-dimethyl-4-silapentane sulfonate sodium salt (DSS). The textural properties of the calcined samples were determined by N_2 adsorption–desorption isotherms at 77 K using a Micromeritics ASAP 2020 system. The total surface area was calculated based on the BET equation. The micropore volume and micropore surface area were evaluated using the *t*-plot method. Thermogravimetry analysis was performed using a TA Q-600 analyzer. The samples were heated from room temperature to 800 °C with a heating rate of 10 °C min^{-1} in an

air flow of 100 ml min^{-1}. XPS measurements were performed using a Thermo ESCALAB 250Xi spectrometer with Al Kα radiation as the excitation source. The surface charge of the sample was calibrated by referencing to the Al 2p peak of Al_2O_3 at 74.7 eV.

The solid yield of the samples was calculated by using the following formula: yield (%) = (M_{sample} × 85%) × 100/($M(Al_2O_3)$ + $M(P_2O_5)$ + $M(SiO_2)$)$_{gel}$, where M_{sample}, 85% and ($M(Al_2O_3)$ + $M(P_2O_5)$ + $M(SiO_2)$)$_{gel}$ stand for the weight of the solid sample, an estimated value of framework compounds included in the sample, and the dry mass of three inorganic oxides in the starting mixture, respectively.

2.3 Modeling method

The Dreiding force field[24,25] was chosen for energy optimization and calculation. Performing the calculations on a siliceous framework instead of $AlPO_4$ is an approximation necessitated by the lack of a suitable force field to describe the organic fragments and the aluminophosphate on an equal footing.[26–28] We believe that this approximation does not interfere with our conclusions, since the flexibility of zeolite and zeotype structures has been shown to depend mostly on the topology of the structure. The atomic charges for the template molecules were calculated by the Mulliken charge distribution method[29] by the quantum chemistry DFT method using the B3LYP functional with 6-31G(*d*,*p*) in GAUSSIAN package, while the charges for the framework O, Si atoms were fixed to −1.05, 2.1.[30] The crystal symmetry was decreased to P1 in order to fit various kinds of organic molecules. In addition, the unit cell and the positions of framework atoms were fixed in the structure optimization progress. The position of the organic species within AFX was obtained by energy minimization based on force-field molecular modelling. The interaction energies (E_{inter}) between the inorganic framework and organic templates are studied. E_{inter} = $E - E_f - E_R$, where E is the total energy of the whole structure, E_f is the energy of the framework, and E_R is the energy of the encapsulated organic template itself. All the calculations about the interaction between the SDAs and the AFX structure were performed using the Gulp code as implemented in Materials Studio software.

3 Results and discussion

3.1 Synthesis and characterization of hollow SAPO-56 nanocrystals

SAPO-56 has been synthesized by amine combination of TEA and TMA instead of its previous template of *N*,*N*,*N*′,*N*′-tetramethyl-1,6-hexanediamine (TMHD).[31] The detailed synthetic conditions and corresponding results are listed in Table 1 and Fig. 1–3 and S1–S3.† As seen in Table 1, without the addition of TMA, SAPO-34 would be the sole product. SAPO-56 appears only if TMA is present in the initial gel. Pure SAPO-56 could be readily achieved when *x*TMA is maintained in the range of 0.3–0.5. When *x*TMA is further increased to 0.6 or higher, dense SAPO-20 crystallizes as the major phase. This is somewhat expected because small molecule TMA^+ has been reported to direct the crystallization of SAPO-20 having only *sod* cages.[32] In addition, lower SiO_2 and HF amounts result in the coexistence of SAPO-34 (Fig. S2†), which will be further discussed in the crystallization process part. It should be mentioned that the present aminothermal environment is essential for the formation of SAPO-56. Too much water in the initial gel (H_2O/Al_2O_3 = 50) would lead to SAPO-34 instead of SAPO-56 (Fig. S3†).

Table 1 The influence of synthetic parameters on the synthesis results

Sample[a]	*x*TMA	*y*SiO_2	*z*HF	Product
1	0	0.5	1.0	SAPO-34
2	0.12	0.5	1.0	SAPO-34 & minor SAPO-56
3	0.2	0.5	1.0	SAPO-56 & minor SAPO-34
4	0.3	0.5	1.0	SAPO-56
5	0.4	0.5	1.0	SAPO-56
6	0.6	0.5	1.0	SAPO-20 & minor SAPO-56
7	0.3	0.3	1.0	SAPO-34 & minor SAPO-56
8	0.3	0.75	1.0	SAPO-56
9	0.3	1.0	1.0	SAPO-56
10	0.3	0.75	0	SAPO-34 & minor SAPO-56
11	0.3	0.75	0.25	SAPO-56 & minor SAPO-34
12	0.3	0.75	0.5	SAPO-56

[a] All samples are prepared under a crystallization temperature of 200 °C for 36 h. The initial molar composition for the inorganic species is as follows: TEA/Al_2O_3/P_2O_5/TMA/SiO_2/HF/H_2O = 7/1/1/*x*/*y*/*z*/10–15.5 (all water in the initial mixtures came from reagents and no extra water was added).

Fig. 1 exhibits the XRD patterns of the as-synthesized samples with different TMA amounts. For samples 4 (0.3TMA) and 5 (0.4TMA), both of them show comparable XRD peak positions with those of SAPO-56 in the literature,[31] indicating their pure phase. The obvious broadness of the peaks

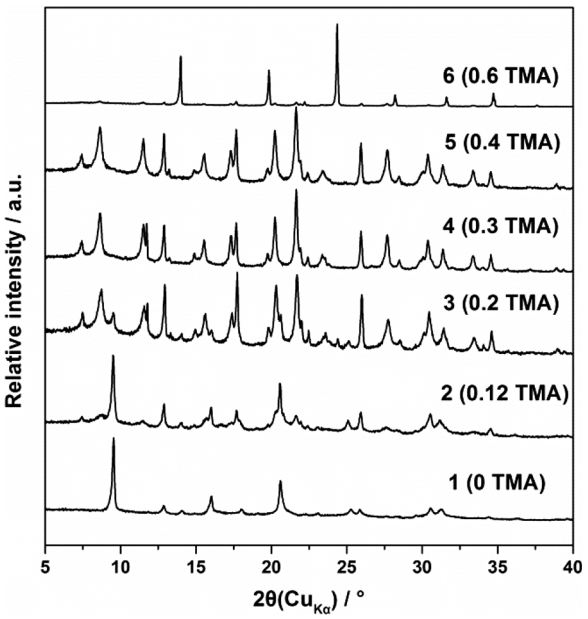

Fig. 1 XRD patterns of the as-synthesized samples with different amounts of TMA.

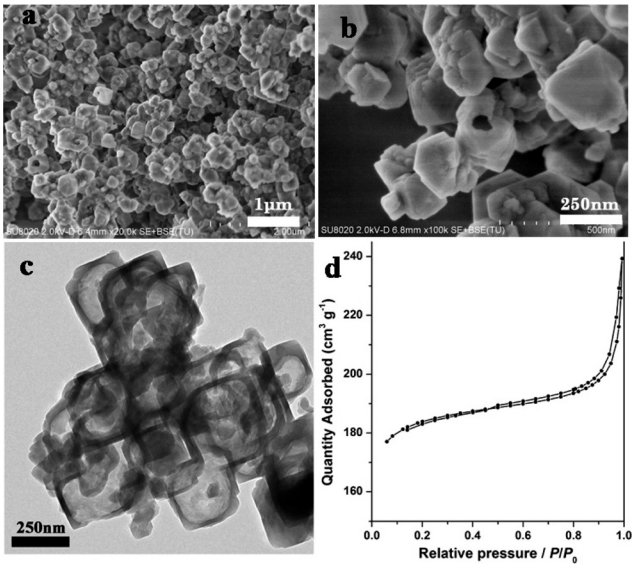

Fig. 2 SEM images of calcined samples 4 (a) and 8 (b), TEM image (c) and N_2 adsorption–desorption isotherms of sample 8 (d).

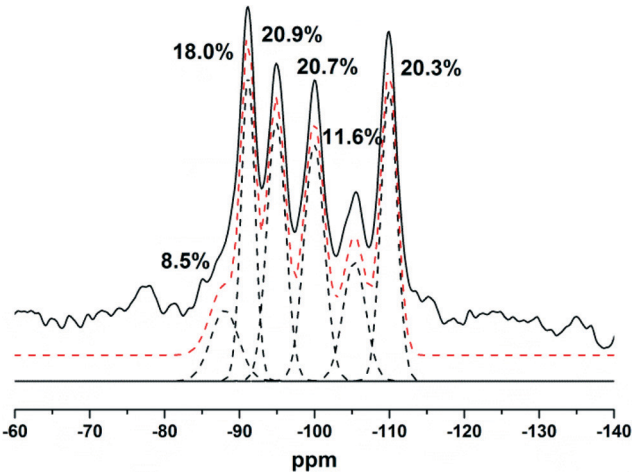

Fig. 3 ^{29}Si MAS NMR of the as-synthesized SAPO-56 (sample 8).

suggests the small crystal size of the samples. SEM was thus used to investigate the crystal morphology (Fig. 2). All SAPO-56 crystals present small particle sizes of 100–500 nm, which are much smaller than that of the conventional hexagonal disk-like SAPO-56.[31,33] Interestingly, an obvious hole can be observed on some crystals. Further observation by TEM (Fig. 2c) reveals that there are large voids inside the crystals, and the shell thickness is *ca.* 40 nm. To our best knowledge, it is the first report concerning the direct synthesis of hollow nano SAPO-56 molecular sieves. Such a hollow morphology with a very thin shell is believed to be favorable for catalytic applications due to the shortened diffusion path, which would facilitate the mass transfer in the catalytic reactions.

The textual properties of the obtained hollow SAPO-56 nanocrystals were characterized by N_2 physical adsorption (Fig. 1d). The sample exhibits a high BET surface area (617 m^2 g^{-1}) and a large micropore volume (0.25 cm^3 g^{-1}), verifying the good crystallinity. The external surface area and total pore volume of the sample are 80 m^2 g^{-1} and 0.33 cm^3 g^{-1}, respectively, owing to the much smaller crystal size and hollow morphology. The abrupt inclination at a relatively high pressure of $P/P_0 > 0.9$ in the isotherms should be associated with the multilayer adsorption inside the void of nanocrystals or/and between the intercrystal pores of nanoparticles.

Solid-state MAS NMR spectra were recorded to investigate the local atomic coordination environments in the as-synthesized SAPO-56 (sample 8, $Al_{0.432}P_{0.339}Si_{0.229}O_2$). The ^{29}Si spectrum presents uncommon quintuplets indicating very complex Si environments (Fig. 3). The signals at −91, −95, −100, −105, and −110 ppm are assigned to Si(4Al), Si(3Al), Si(2Al), Si(1Al) and Si-islands (Si(0Al)), respectively. Additionally, a weak peak at around −85 ppm is present, which possibly arises from $Si(OAl)_3(OH)$ or $Si(OAl)(OSi)(OH)_2$ species from the breaking of some Si–OH–Al bonds, disordered Si(4Al) or partially hydrated Si species located at the edge of the Si domain.[34] According to the deconvolution analysis for the spectrum, the amount of Si(*n*Al) (n = 0–3) accounts for 72.5%, which is quite higher than that of conventional SAPO molecular sieves and suggests the existence of large Si islands and Si–Al domains in the framework of hollow SAPO-56. The ^{27}Al and ^{31}P MAS NMR spectra are presented in Fig. S4.† Two peaks centred at around 39 and 11 ppm are observed in the ^{27}Al spectrum, which are assigned to the tetra- and penta-coordinated Al species in the framework. The ^{31}P spectrum gives one strong resonance peak at −29.5 ppm attributable to the P(4Al) environment.[35]

3.2 Co-templating investigation

^{13}C MAS NMR was used to identify the exact template species occluded in the sample. As shown in Fig. 4, the peak centered at 48 ppm can be ascribed to the $-CH_3$ groups of TMA and/or $-CH_2-$ groups of TEA. The signal at 9.5 ppm confirms the presence of TEA which arises from the $-CH_3$ groups of TEA. The two peaks are integrated, and their ratio is

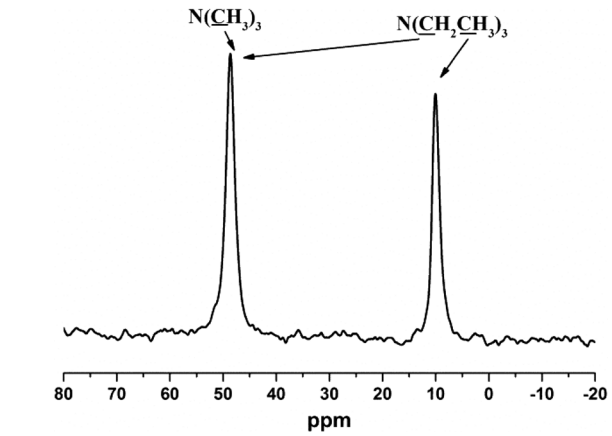

Fig. 4 ^{13}C MAS NMR spectrum of as-synthesized sample 8.

calculated to be about 3 : 2. If there is only a TEA template, the ratio should be close to 1 : 1. The present results suggest the coexistence of TMA and TEA in the solid, and the TEA/TMA molar ratio is around 2 : 1.

Thermal analysis (Fig. S5†) was measured to examine the organic content in the sample. The first weight loss of 4.2 wt% below 150 °C corresponds to the desorption of water. The weight loss of 16.1 wt% between 150–600 °C, accompanied by an obvious exothermic peak at 440 °C in the DSC curve, is attributed to the decomposition of organic molecules occluded within the crystals. Based on the TG, NMR and XRF results, the number of TEA and TMA molecules per SAPO-56 unit cell is calculated to be 4.4 and 2.2, respectively. The unit cell composition for SAPO-56 (sample 8) could be expressed as $(TEA)_{4.4}(TMA)_{2.2}(H_2O)_{8.5}[Al_{20.7}P_{16.3}Si_{11.0}O_{96}]$.

Given that SAPO-56 has an AFX topology containing both small *gme* and large *aft* cages in equivalent number (two sets of *gme* and *aft* cages in each unit cell) and the TEA molecule has a large volume, we speculated that each of the *aft* and *gme* cages may be occupied by two TEA and one TMA, respectively. Theoretical calculation is further employed to verify the conjecture, and an AFX siliceous framework model was therefore built up to evaluate the interaction energies of the SDAs with the AFX framework. The position of the organic species was determined by energy minimization based on force-field molecular modeling. The detailed interaction energies for the amines in different cavities are given in Table S1.† It is found that TEA molecules are too large to be put in the *gme* cage. They can only stay in the large *aft* cage, and two TEA molecules per *aft* cage have the lowest energy. For TMA, it may be occluded in both cages due to the small volume. The average adsorbed energy for one TMA in an *aft* cage is −14.9 kcal mol^{-1} and the value for one TEA in an *aft* cage is −26.6 kcal mol^{-1}, suggesting that TEA molecules enter *aft* cages preferentially when both TMA and TEA coexist. On the basis of the calculation results in Table S1,† it is shown that the most stable status in the as-made AFX material should be two TEA molecules and one TMA in the *aft* and *gme* cages, respectively, supporting our speculation well. The calculated interaction energy per unit cell is −136.90 kcal mol^{-1}. Fig. 5 illustrates the optimal locations and conformations of the amines in the cages, showing the collaboration of TEA and TMA on the formation of SAPO-56.

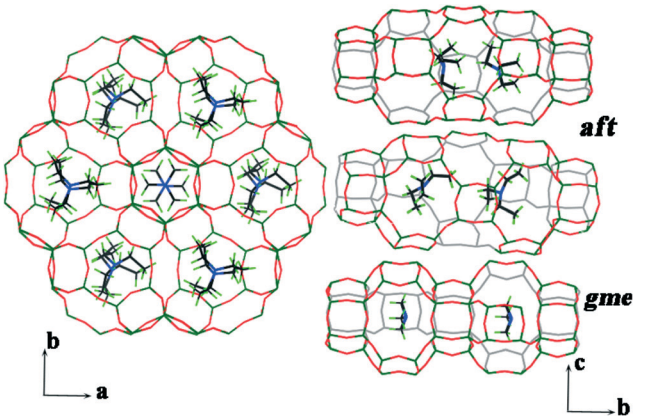

Fig. 5 Projection of the AFX structure viewed along the [001] direction (left) and the locations and conformations of the TEA and TMA amines occluded in the cages (right). Each unit cell in the AFX structure contains two different sets of *aft* and *gme* cages corresponding to two different TEA and TMA conformations in the *aft* and *gme* cages.

3.3 Crystallization process

A series of time-dependent syntheses based on the synthetic conditions of sample 8 were conducted for a better understanding of the crystallization process and mechanism. The XRD patterns of the samples are displayed in Fig. 6. The corresponding SEM images are shown in Fig. 7. It can be seen that cubic-like SAPO-34 with an uneven surface first forms within 2.33 hours. Afterwards, some nano-grains start to appear on the surface of SAPO-34 crystals. As the amount of nano-grains increased, weak XRD peaks (labeled by "*" in Fig. 6) besides those of SAPO-34 could be detected at 4.23 h. These weak peaks gradually become stronger as the reaction continues and can be indexed to the AFX structure. Meanwhile, the morphology of SAPO-34 changes to a sandwich shape, suggesting an etching of the crystals. At 12 h, the XRD peaks arising from SAPO-34 become weaker and almost invisible. Correspondingly, only SAPO-56 nanoparticles with a size of 100–500 nm exist in the solid. Moreover, obvious holes can be observed in some nanocrystals. When the crystallization time was further prolonged to 24 h or longer, there is less change in the XRD pattern, crystal morphology and solid yield, indicating the completion of the crystallization.

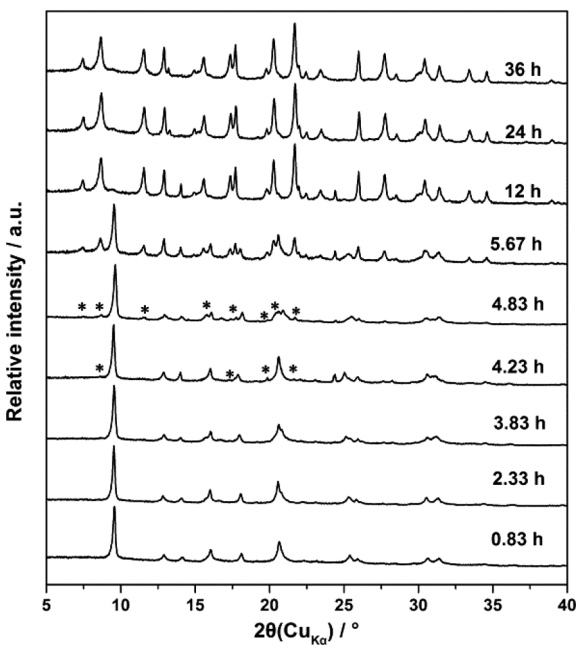

Fig. 6 XRD patterns of the samples synthesized with different crystallization times.

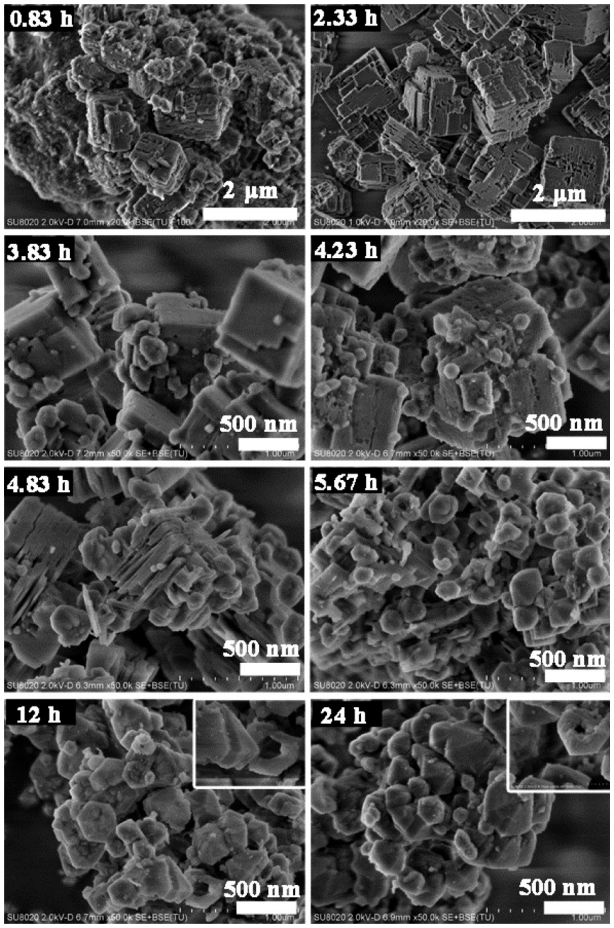

Fig. 7 SEM images of the calcined samples synthesized with different crystallization times.

The compositions of the products with different crystallization times are monitored by XRF (Table 2). The initial solids with SAPO-34 as the major phase have low Si incorporation. It is reasonable because only TEA is included in SAPO-34 (see Fig. S6†), and it generally leads to low silica SAPO-34 (Si/(Si + Al + P) < 0.15).[36] The silica content in the solids increases with increasing percentage of SAPO-56. Because of the higher charge density and smaller size of TMA, much more silica was supposed to be involved in the crystallization so that the positive charges caused by the protonated TMA can be balanced. This speculation is also consistent (Table 1). That is, a higher Si content in the gel facilitates the synthesis of pure SAPO-56. Otherwise, a mixture of SAPO-34 and SAPO-56 would be obtained. In addition, a small amount of F element was detected in the intermediate product (2.33–12 h), which has proven to be helpful for the crystallization of Si-poor SAPO-34 or even AlPO-34.[37] The ^{19}F MAS NMR of sample 2.33 h (Fig. S7†) further confirms the presence of fluoride. The single resonance peak centered at −128 ppm is attributed to the bridged F atoms connected to two Al atoms.[38] The F^- ions disappear gradually as SAPO-56 appears. In addition, no F can be detected by the XRF and ^{19}F MAS NMR for sample 36 h. However, HF is indispensible for the formation of the pure SAPO-56 phase under the current conditions. Without the addition of HF, the product would turn to SAPO-34 with minor SAPO-56 (sample 10).

Table 2 Changes in the solid phases during the phase transformation process

Time	Products	Yield (%)	Product composition
0.83 h	SAPO-34 & amorphous	22.3	N/A
2.33 h	SAPO-34	27.2	$Al_{0.462}P_{0.437}Si_{0.072}F_{0.029}O_2$
3.83 h	Minor SAPO-56 & SAPO-34	27.9	$Al_{0.464}P_{0.439}Si_{0.071}F_{0.026}O_2$
4.23 h	Minor SAPO-56 & SAPO-34	29.6	$Al_{0.465}P_{0.440}Si_{0.070}F_{0.024}O_2$
4.83 h	Minor SAPO-56 & SAPO-34	32.5	$Al_{0.478}P_{0.425}Si_{0.081}F_{0.016}O_2$
5.67 h	SAPO-56 & SAPO-34	35.5	$Al_{0.463}P_{0.403}Si_{0.118}F_{0.016}O_2$
12 h	SAPO-56 & minor SAPO-34	47.4	$Al_{0.449}P_{0.359}Si_{0.176}F_{0.016}O_2$
24 h	SAPO-56	49.5	$Al_{0.441}P_{0.345}Si_{0.214}O_2$
36 h	SAPO-56	50.2	$Al_{0.432}P_{0.339}Si_{0.229}O_2$

It is interesting to observe the *in situ* phase transformation of SAPO-34 to SAPO-56 in the present aminothermal synthesis. The transition is related to the phase selectivity issue, which is a fundamental question, but still not well understood presently. Generally, it is acknowledged that molecular sieves are metastable materials, which crystallize through kinetic control and may transform into more stable products following Ostwald ripening.[39] However, herein, SAPO-34 and SAPO-56 have a similar framework density of 14.5 and 14.7 T/1000 Å^3, respectively. Zicovich-Wilson *et al.* once investigated the *in situ* transformation of TON to less dense ITW by periodic *ab initio* calculations. They concluded that structure directing agents do not "choose" a structure kinetically but through stabilization.[40,41] This can be applied to explain the present observation. That is, host–guest interactions between the templates (TEA and TMA) and the SAPO-56 framework are stronger than the interactions of (TEA + F^-) and the SAPO-34 framework, which thus induces the evolution of the phase transition.

Based on the above results, the formation process of SAPO-56 nanocrystals is proposed and illustrated in Scheme 1.

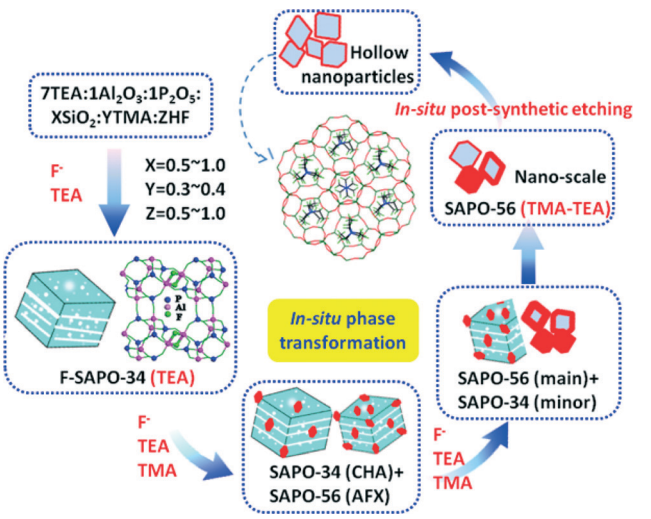

Scheme 1 Schematic presentation of the proposed phase transformation and hollow structure formation process.

At the early stage of the crystallization, Si-poor SAPO-34 first forms with the help of TEA and F^-. This phase is not actually stable under the present synthetic conditions. The surface of SAPO-34 crystals is gradually etched by F^- ions together with organic amines. At the same time, SAPO-56 starts to nucleate on the surface of SAPO-34 crystals through the collaboration of TEA and TMA. As the reaction continues, the phase of SAPO-56 increases at the expense of SAPO-34. In addition, the crystallization rate of SAPO-56 is much faster than the dissolution of SAPO-34, as evidenced by the continuously increasing solid yields with time. Possibly, the structural fragments from the dissolution of SAPO-34 participate in the nucleation and growth of SAPO-56 crystals and thus hasten the formation rate of SAPO-56. The observed *in situ* phase transformation process from SAPO-34 to SAPO-56 is believed to result from the stronger host–guest interactions in the latter material, which make its formation energetically more favorable than the former.

3.4 Formation of hollow SAPO-56 nanocrystals

Hollow-structured materials have currently attracted great attention due to their potential applications in catalysis, drug delivery and so on.[42,43] Although many strategies have been developed to prepare hollow molecular sieves, the direct synthesis route still remains a difficult task. In addition, most of the successful examples by complex layer-by-layer assembly or post-synthetic alkaline treatment are limited to aluminosilicate zeolites.[44,45] There are fewer reports on the direct preparation of hollow SAPO materials and their formation mechanism.

To figure out the reason for the hollow morphology formation of SAPO-56, samples with different crystallization times are first examined by TEM (Fig. 8). It can be seen that the hollow phenomenon of SAPO-56 nanocrystals does not appear until the crystallization of 12 h. Afterwards, more and more hollow crystals appear and the thickness of the shell becomes thinner with increasing crystallization time. At 24 h, most of the crystals become hollow, which is comparable with the sample crystallized for 36 h. These results reveal that the hollow structure of SAPO-56 crystals is not created during their formation but by *in situ* post-synthetic etching (Scheme 1).

Besides the reaction time, we also found that the formation of a hollow structure has a close relationship with the concentration of HF. The TEM images of the samples synthesized with different amounts of HF are presented in Fig. 9. For sample 10 (0HF), minor SAPO-56 is attached on the SAPO-34 crystal surface. There is no hollow phenomenon that can be found for SAPO-56 nanocrystals. The large voids observed in the interior of SAPO-34 crystals are possibly due to the alkaline leaching.[46] With the addition of HF, the corrosion of SAPO-34 crystals becomes severe and some SAPO-56 crystals show the hollow structure. The coexistence of hollow and solid crystals in the sample suggests that the properties of SAPO crystals are inhomogeneous, even if they are from the same batch. For sample 12 (0.5HF), SAPO-34 crystals are almost invisible and much more SAPO-56 crystals became hollow. When the HF/Al_2O_3 ratio is increased to 1.0 (sample 8, Fig. 1c), nearly all the SAPO-56 crystals become hollow with a similar shell thickness of *ca.* 40 nm.

It is speculated that both the alkaline environment and the existence of fluoride are important to the creation of hollow-structured SAPO-56. First, we discuss the effect of alkaline leaching on the formation of a hollow morphology. Post-synthetic alkaline extraction has been reported to achieve hollow ZSM-5, besides its common use for the

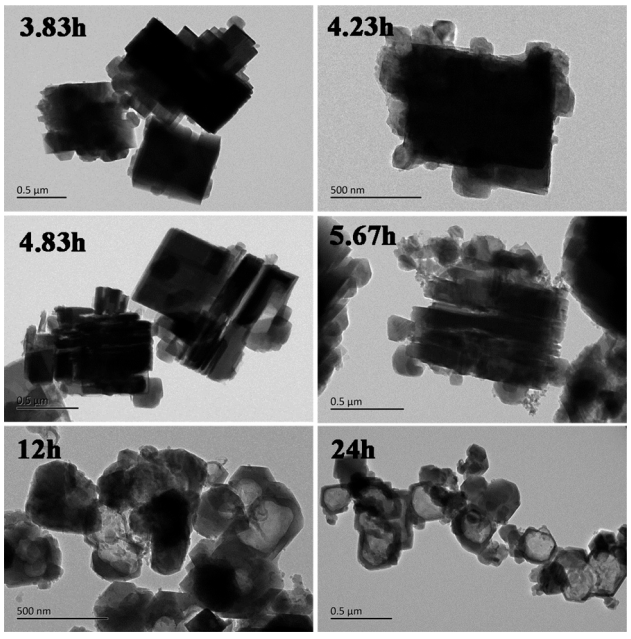

Fig. 8 TEM images of the samples synthesized with different crystallization times.

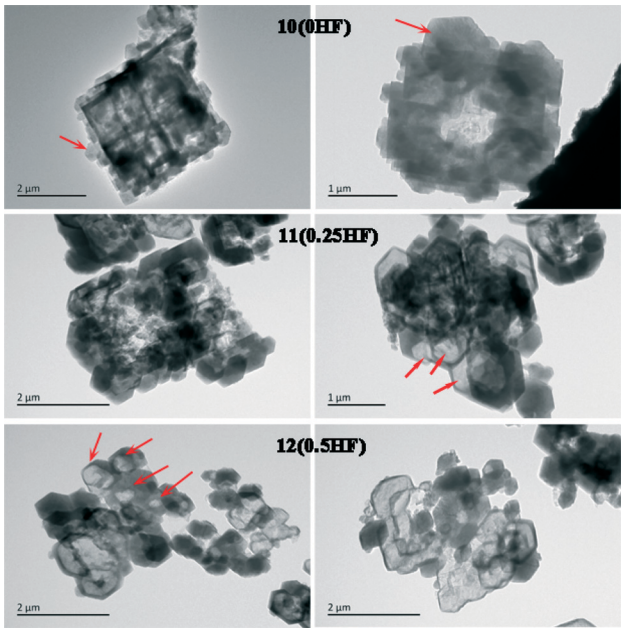

Fig. 9 TEM images of as-synthesized samples 10 (0HF), 11 (0.25HF) and 12 (0.5HF).

preparation of mesoporous zeolites. The Al gradient in the crystals (Al-rich exterior) is proposed to be responsible for the formation of hollow particles,[47] because Al atoms have better resistance to alkaline extraction and they can offer a protection to Si atoms around themselves. However, for SAPO molecular sieves, they generally have a Si-rich outer layer.[48–50] In addition, the XPS characterization for hollow SAPO-56 also gives a surface Si enrichment result with a composition of $Al_{0.372}P_{0.276}Si_{0.352}O_2$ as compared to the bulk composition of $Al_{0.432}P_{0.339}Si_{0.229}O_2$. Recently, Verboekend *et al.* have generalized the stability of chemical bonds in basic media in the order of Al–O–Si ≫ Si–O–Si > Al–O–P,[46] which means that the Al–O–P parts of SAPO molecular sieves are preferentially attacked by the alkaline environment, and the Si enriched parts containing more Al–O–Si bonds have better stability. It is thus supposed that the interior of SAPO-56 with a relatively lower Si content (more Al–O–P bonds) has a poorer resistance to the base leaching and the shell with enriched Si–O–Al bonds is preserved finally. Moreover, the very special ^{29}Si NMR of hollow SAPO-56 (Fig. 3) suggests that the stable microenvironments of the SAPO framework in base media is the coexistence of various Si species with abundant Si–O–Al connection, in agreement with the above analysis.

The formation of hollow SAPO-56 is also attributed to the presence of HF. According to the literature, there exist various fluoride species in the solution such as F^-, HF, HF_2^-, $H_2F_3^-$ *etc.* depending on the fluoride concentration and environment.[51] A previous study reported that diluted HF acid preferentially extracts aluminum from zeolite frameworks, where free F^- ions have the highest activity and the undissociated HF molecules and HF_2^- responsible for silicon removal could be ignored.[52] It is also proved by Vistad *et al.* that there are only free F^- ions under alkaline conditions.[53] Therefore, under our aminothermal system, dealumination rather than desilication by free F^- ions is the most possible etching process, which works together with the alkaline extraction to create the hollow morphology.

Conclusions

SAPO-56 nanocrystals with a hollow morphology have been synthesized by a HF-assisted aminothermal co-templating method. The aminothermal environment and the coexistence of TMA and TEA amines are important for the crystallization of SAPO-56, in which 1TMA and 2TEA stay in the small *gme* and large *aft* cavities, respectively, to make the AFX structure stable. Investigation on the crystallization process reveals that there exists an *in situ* phase transformation process from F-SAPO-34 (with TEA as the template) to SAPO-56, which is followed by a further *in situ* post-synthetic leaching to generate the hollow structure of SAPO-56. Both the alkaline medium and the fluoride ions may contribute to the corrosion of SAPO-34 and the creation of the hollow-structured SAPO-56. Abundant Si coordination species (more Si–O–Al bonds and less Al–O–P bonds) in the outer layer of the SAPO-56 crystals help the shell survive from the etching of HF–TMA–TEA environment. This work demonstrates that the aminothermal co-templating strategy is a promising route to explore the synthesis of SAPO molecular sieves. In the future, more works including experiments and theoretical calculations need to be performed to understand the possible matching rules between amines under the aminothermal environment. Meanwhile, the effect of F^- ions cannot be ignored, which may exert an influence on the crystallization pathway. More interesting SAPO molecular sieves are expected to be prepared by this novel route.

Acknowledgements

We are thankful for the financial support from the National Natural Science Foundation of China (21476228).

Notes and references

1 M. E. Davis, *Nature*, 2002, **417**, 813–821.
2 A. Corma, *Chem. Rev.*, 1997, **97**, 2373–2420.
3 M. E. Davis and R. F. Lobo, *Chem. Mater.*, 1992, **4**, 756–768.
4 R. F. Lobo, M. Pan, I. Chan, H.-X. Li, R. C. Medrud, S. I. Zones, P. A. Crozier and M. E. Davis, *Science*, 1993, **262**, 1543–1546.
5 S. I. Zones, S. J. Hwang and M. E. Davis, *Chem. – Eur. J.*, 2001, **7**, 1990–2001.
6 J. Y. Li, A. Corma and J. H. Yu, *Chem. Soc. Rev.*, 2015, **44**, 7112–7127.
7 V. R. R. Marthala, M. Hunger, F. Kettner, H. Krautscheid, C. Chmelik, J. R. Kärger and J. Weitkamp, *Chem. Mater.*, 2011, **23**, 2521–2528.
8 Y. Wei, Z. J. Tian, H. Gies, R. R. Xu, H. J. Ma, R. Y. Pei, W. P. Zhang, Y. P. Xu, L. Wang, K. D. Li, B. C. Wang, G. D. Wen and L. W. Lin, *Angew. Chem., Int. Ed.*, 2010, **49**, 5367–5370.
9 L. P. Ye, F. H. Cao, W. Y. Ying, D. Y. Fang and Q. W. Sun, *J. Porous Mater.*, 2010, **18**, 225–232.
10 N. Najafi, S. Askari and R. Halladj, *Powder Technol.*, 2014, **254**, 324–330.
11 P. Tian, Y. Wei, M. Ye and Z. Liu, *ACS Catal.*, 2015, **5**, 1922–1938.
12 A. B. Pinar, L. Gomez-Hortiguela and J. Perez-Pariente, *Chem. Mater.*, 2007, **19**, 5617–5626.
13 R. S. Xu, W. P. Zhang, J. Guan, Y. P. Xu, L. Wang, H. J. Ma, Z. J. Tian, X. W. Han, L. W. Lin and X. H. Bao, *Chem. – Eur. J.*, 2009, **15**, 5348–5354.
14 Y. Wei, B. Marler, L. Zhang, Z. Tian, H. Graetsch and H. Gies, *Dalton Trans.*, 2012, **41**, 12408–12415.
15 M. Castro, R. Garcia, S. J. Warrender, A. M. Slawin, P. A. Wright, P. A. Cox, A. Fecant, C. Mellot-Draznieks and N. Bats, *Chem. Commun.*, 2007, 3470–3472, DOI: 10.1039/b705377k.
16 M. Briend, A. Lamy, M.-J. Peltre, P. P. Man and D. Barthomeuf, *Zeolites*, 1993, **13**, 201–211.
17 H. Z. Xing, J. Y. Li, W. F. Yan, P. Chen, Z. Jin, J. H. Yu, S. Dai and R. R. Xu, *Chem. Mater.*, 2008, **20**, 4179–4181.

18 G. J. Lewis, M. A. Miller, J. G. Moscoso and B. A. Wilson, *U.S. Pat.* 7578993, 2009.
19 M. B. Park, Y. Lee, A. Zheng, F.-S. Xiao, C. P. Nicholas, G. J. Lewis and S. B. Hong, *J. Am. Chem. Soc.*, 2012, **135**, 2248–2255.
20 D. Fan, P. Tian, S. T. Xu, Q. H. Xia, X. Su, L. Zhang, Y. Zhang, Y. L. He and Z. M. Liu, *J. Mater. Chem.*, 2012, **22**, 6568.
21 D. Fan, P. Tian, X. Su, Y. Y. Yuan, D. H. Wang, C. Wang, M. Yang, L. Y. Wang, S. T. Xu and Z. M. Liu, *J. Mater. Chem. A*, 2013, **1**, 14206–14233.
22 D. H. Wang, P. Tian, M. Yang, S. T. Xu, D. Fan, X. Su, Y. Yang, C. Wang and Z. M. Liu, *Microporous Mesoporous Mater.*, 2014, **194**, 8–14.
23 D. H. Wang, P. Tian, D. Fan, M. Yang, B. B. Gao, Y. Y. Qiao, C. Wang and Z. M. Liu, *J. Colloid Interface Sci.*, 2014, **445C**, 119–126.
24 J. H. Yu, J. Y. Li, K. X. Wang, R. R. Xu, K. Sugiyama and O. Terasaki, *Chem. Mater.*, 2000, **12**, 3783–3787.
25 J. Y. Li, J. H. Yu and R. R. Xu, *Microporous Mesoporous Mater.*, 2007, **101**, 406–412.
26 M. Zokaie, D. S. Wragg, A. Grønvold, T. Fuglerud, J. H. Cavka, K. P. Lillerud and O. Swang, *Microporous Mesoporous Mater.*, 2013, **165**, 1–5.
27 A. Sartbaeva, S. A. Wells, M. M. J. Treacy and M. F. Thorpe, *Nat. Mater.*, 2006, **5**, 962–965.
28 V. Kapko, C. Dawson, M. M. J. Treacy and M. F. Thorpe, *Phys. Chem. Chem. Phys.*, 2010, **12**, 8531–8541.
29 G. Sastre, A. Cantin, M. J. Diaz-Cabañas and A. Corma, *Chem. Mater.*, 2005, **17**, 545–552.
30 Y. G. Bushuev and G. Sastre, *J. Phys. Chem. C*, 2009, **113**, 10877–10886.
31 S. T. Wilson, R. W. Broach, C. S. Blackwell, C. A. Bateman, N. K. McGuire and R. M. Kirchner, *Microporous Mesoporous Mater.*, 1999, **28**, 125–137.
32 S. B. Hong, *Microporous Mater.*, 1995, **4**, 309–317.
33 Z. Z. Xie, M. Q. Zhu, A. Nambo, J. B. Jasinski and M. A. Carreon, *Dalton Trans.*, 2013, **42**, 6732–6735.
34 Z. B. Li, J. Martínez-Triguero, P. Concepción, J. H. Yu and A. Corma, *Phys. Chem. Chem. Phys.*, 2013, **15**, 14670–14680.
35 A. Buchholz, W. Wang, A. Arnold, M. Xu and M. Hunger, *Microporous Mesoporous Mater.*, 2003, **57**, 157–168.
36 L. Xu, A. P. Du, Y. X. Wei, Y. L. Wang, Z. X. Yu, Y. L. He, X. Z. Zhang and Z. M. Liu, *Microporous Mesoporous Mater.*, 2008, **115**, 332–337.
37 A. Tuel, S. Caldarelli, A. Meden, L. B. McCusker, C. Baerlocher, A. Ristic, N. Rajic, G. Mali and V. Kaucic, *J. Phys. Chem. B*, 2000, **104**, 5697–5705.
38 Z. M. Yan, B. H. Chen and Y. N. Huang, *Solid State Nucl. Magn. Reson.*, 2009, **35**, 49–60.
39 I. Goto, M. Itakura, S. Shibata, K. Honda, Y. Ide, M. Sadakane and T. Sano, *Microporous Mesoporous Mater.*, 2012, **158**, 117–122.
40 C. M. Zicovich-Wilson, F. Gándara, A. Monge and M. A. Camblor, *J. Am. Chem. Soc.*, 2010, **132**, 3461–3471.
41 A. Rojas, M. L. San-Roman, C. M. Zicovich-Wilson and M. A. Camblor, *Chem. Mater.*, 2013, **25**, 729–738.
42 N. Ren, Y.-H. Yang, Y.-H. Zhang, Q.-R. Wang and Y. Tang, *J. Catal.*, 2007, **246**, 215–222.
43 Y. Zhu, J. Shi, W. Shen, X. Dong, J. Feng, M. Ruan and Y. Li, *Angew. Chem.*, 2005, **117**, 5213–5217.
44 K. H. Rhodes, S. A. Davis, F. Caruso, B. Zhang and S. Mann, *Chem. Mater.*, 2000, **12**, 2832–2834.
45 C. Y. Dai, A. F. Zhang, L. L. Li, K. K. Hou, F. S. Ding, J. Li, D. Y. Mu, C. S. Song, M. Liu and X. W. Guo, *Chem. Mater.*, 2013, **25**, 4197–4205.
46 D. Verboekend, M. Milina and J. Perez-Ramirez, *Chem. Mater.*, 2014, **26**, 4552–4562.
47 C. S. Mei, Z. C. Liu, P. Y. Wen, Z. K. Xie, W. M. Hua and Z. Gao, *J. Mater. Chem.*, 2008, **18**, 3496–3500.
48 S. A. Schunk, D. G. Demuth, B. Schulz-Dobrick, K. K. Unger and F. Schüth, *Microporous Mater.*, 1996, **6**, 273–285.
49 A. K. Sinha and S. Seelan, *Appl. Catal., A*, 2004, **270**, 245–252.
50 G. Y. Liu, P. Tian, Y. Zhang, J. Z. Li, L. Xu, S. H. Meng and Z. M. Liu, *Microporous Mesoporous Mater.*, 2008, **114**, 416–423.
51 K. W. Kolasinski, *J. Electrochem. Soc.*, 2005, **152**, J99–J104.
52 Z. Qin, L. Lakiss, J.-P. Gilson, K. Thomas, J.-M. Goupil, C. Fernandez and V. Valtchev, *Chem. Mater.*, 2013, **25**, 2759–2766.
53 Ø. Vistad, E. Hansen, D. Akporiaye and K. Lillerud, *J. Phys. Chem. A*, 1999, **103**, 2540–2552.

